The Astrophysical Journal, 668:839–845, 2007 October 20

THE GALAXY LUMINOSITY FUNCTION AT $z \simeq 1$ IN THE HUDF: PROBING THE DWARF POPULATION[1]

R. E. Ryan, Jr.,[2] N. P. Hathi,[2] S. H. Cohen,[3] S. Malhotra,[3] J. Rhoads,[3]
R. A. Windhorst,[3] T. Budavári,[4] N. Pirzkal,[5] C. Xu,[5]
N. Panagia,[6] L. A. Moustakas,[7] S. di Serego Alighieri,[8] and H. Yan[9]
Received 2007 March 2; accepted 2007 April 9

ABSTRACT

We present a catalog of spectrophotometric redshifts for 1308 galaxies from the Grism ACS Program for Extragalactic Science (GRAPES) observations with the *Hubble Space Telescope*. These low-resolution spectra between 6000 Å and 9500 Å are supplemented with U, J, H, and K_s data from various facilities, resulting in redshifts computed with ~40 spectral bins per galaxy. For 75 galaxies in the range $0.5 < z < 1.5$ with spectroscopic redshifts, the standard deviation in the fractional error in $1 + z$ is 0.037. With this catalog, we compute the B-band luminosity function in this redshift range from 72 galaxies. Due to the depth of the GRAPES survey, we are able to accurately constrain the faint-end slope by going to $M_B \simeq -18$ mag at $z = 1.0 \pm 0.2$, nearly 2 mag fainter than previous studies. The faint-end slope is $\alpha = -1.32 \pm 0.07$. When compared to numerous published values at various redshifts, we find strong evidence for a steepening of the faint-end slope with redshift, which is expected in the hierarchical formation scenario of galaxies.

Subject headings: catalogs — galaxies: high-redshift — surveys

Online material: machine-readable table

1. INTRODUCTION

Measuring a large sample of accurate redshifts for distant galaxies is one of the most daunting tasks in observational cosmology and extragalactic science. Given the typical brightness (AB ~ 26 mag) of distant ($z \gtrsim 1$) galaxies, optical spectroscopy requires extensive observations on the largest telescopes. While multislit spectrographs and grating prism (grism) modes allow for many simultaneous spectroscopic observations, they can be severely limited in wavelength coverage and spectral resolution. Therefore, the use of photometric redshifts estimated from observed fluxes is a necessity for the statistical study of distant galaxies (e.g., Grazian et al. 2006; Coe et al. 2006; Mobasher et al. 2007).

Since the release of the original Hubble Deep Field (HDF; Williams et al. 1996), photometric redshifts have been the focus of numerous studies and are the cornerstone of many others. At present, there are primarily two different, yet similar techniques for computing these redshifts: χ^2 minimization and Bayesian statistics. The minimization scheme compares a set of model fluxes measured from empirical or synthetic spectral energy distributions (SEDs) to the observed fluxes. The earliest mature studies using χ^2 minimization were met with some skepticism regarding possible degeneracies between redshift and internal reddening in galaxy colors (Lanzetta et al. 1996). With the addition of near-infrared (*JHK*) imaging in the HDF, Fernández-Soto et al. (1999) showed that many of the degeneracies can be broken to yield fairly accurate redshifts ($\sigma[\Delta z/(1 + z_{\rm spec})] \approx 0.1$). In contrast, the Bayesian marginalization uses prior redshift probabilities, obtained by other means, to compute extremely accurate redshifts (Benítez 2000). While the current implementation of this technique, BPZ, produces reliable redshifts from limited observational constraints, it does not compute many useful quantities (e.g., k-corrected magnitudes, probability densities, V-band extinction, and age; Caputi et al. 2004).

The luminosity function (LF) of galaxies represents the distribution of galaxy luminosities in a redshift interval. Since the LF can be used to constrain galaxy formation models, it has been well studied at both high and low redshifts. While the LF can be computed at any wavelength, it is often studied in the rest-frame B bandpass. At $z \simeq 1$, accurate determination of the B-band LF requires large, deep surveys (Chen et al. 2003; Abraham et al. 2004; Cross et al. 2004; Zucca et al. 2006). In this work, we complement these studies by going nearly 2 mag fainter in M_B and accurately determining the shape of the LF, particularly the faint-end slope.

Where necessary, we assume the *Wilkinson Microwave Anisotropy Probe* cosmology (*WMAP*; Spergel et al. 2007), where $\Omega_0 = 0.26$, $\Omega_\Lambda = 0.74$, and $H_0 = 73$ km s^{-1} Mpc^{-1}. All magnitudes quoted herein are in the AB system (Oke & Gunn 1983). This paper is organized as follows: the data are described in § 2, the details of the redshift measurements are given in § 3, the redshift quality and luminosity function are described in § 4, and a discussion of the results is given in § 5.

2. OBSERVATIONS

The Grism ACS Program for Extragalactic Science (GRAPES; Pirzkal et al. 2004) data consist of 40 orbits' worth of observations with the *Hubble Space Telescope* (*HST*) of the Hubble Ultra Deep Field (HUDF; Beckwith et al. 2006) during Cycle 12. These

[1] Based on observations made with the NASA/ESA *Hubble Space Telescope*, obtained from the Data Archive at the Space Telescope Science Institute, which is operated by the Association of Universities for Research in Astronomy, Inc., under NASA contract NAS 5-26555.

[2] Department of Physics, Arizona State University, Tempe, AZ 85287; russell.ryanjr@asu.edu.
[3] School of Earth and Space Exploration, Arizona State University, Tempe, AZ 85287.
[4] Department of Physics and Astronomy, Johns Hopkins University, Baltimore, MD 21218.
[5] Shanghai Institute of Technical Physics, 500 Yutian Road, Shanghai 200083, China.
[6] Space Telescope Science Institute, Baltimore, MD 21218.
[7] Jet Propulsion Laboratory, California Institute of Technology, Pasadena, CA 91109.
[8] INAF–Osservatorio Astrofisico di Arcetri, Largo Enrico Fermi 5, I-50125 Florence, Italy.
[9] California Institute of Technology, Pasadena, CA 91125.

slitless spectroscopic data were taken with the Advanced Camera for Surveys (ACS) in the G800L mode and range from ~5500 to 10500 Å with a resolution of $R \simeq 100$, covering $\simeq$11 arcmin^2. The GRAPES observations were taken over four epochs, each with a different position angle in order to minimize the contamination from nearby objects. These data were supplemented with the existing grism observations of Riess et al. (2004), giving a total data set of five position angles and an integration time of 1.1×10^5 s. A thorough discussion of the GRAPES observations, data reduction, and spectral extraction and calibration can be found in Pirzkal et al. (2004).

2.1. *Additional Bandpasses*

Given the limited spectral range of the GRAPES observations, it is necessary to include the existing broadband data available in this highly observed field to increase accuracy of the redshift measurements. To extend our spectra to ~3000 Å–2.3 μm, we include the CTIO MOSAIC II *U*-band observations, the *HST* NICMOS *J*- and *H*-band data (Thompson et al. 2005), and VLT ISAAC K_s-band data. Therefore, the final data set has ~40 independent spectral points from the combination of broadband and grism observations.

Since the i'-band image is the deepest optical exposure ever taken, it is used to define the apertures for the near-ultraviolet (NUV) and near-infrared (NIR) data. To eliminate aperture corrections between the broadband data, we convolve all images to the same FWHM as the worst observation (the *U*-band data), which is 1.3″. While convolving the *HST* images is highly undesirable, the NUV constraint is essential to accurately determine the redshifts at $1 \lesssim z \lesssim 2.3$ (Ferguson 1999). Stanway et al. (2003) suggest that surveys with *U*- and *B*-band data can expect drastically reduced catastrophic failures for galaxies, while quasar colors remain degenerate and the redshifts may be unreliable. Since the point-spread function (PSF) is $\simeq$20 times larger for the ground-based observations, many objects in the *HST* images become confused after the convolution. Objects were deemed confused if, after the convolution, >1 object from the original GRAPES catalog (Pirzkal et al. 2004) was within the new aperture. Therefore, *U*-band flux was only measured for galaxies that have unconfused detections; the remaining galaxies were only measured from the unconvolved images and do not have a *U*-band measurement.

The final photometric data set includes 1308 galaxies with grism spectroscopy. Since the *HST* NICMOS data cover ~50% of the HUDF observed with the ACS, 687 out of 1308 galaxies have *J*- and *H*-band imaging, and only 543 out of 1308 galaxies have *viable* *U*-band data. In total, 273 out of 1308 galaxies have the entire suite of *UB* plus grism plus JHK_s data. All broadband magnitudes are measured as MAG_AUTO by SExtractor in dual-image mode with the default values for PHOT_AUTOPARAMS (Bertin & Arnouts 1996). To determine the apertures, we use DETECT_THRESH and ANALYSIS_THRESH values of 1.5.

2.2. *Source Catalogs*

For the matched aperture photometry, we use the convolved *HST* ACS i' band as the *detection image* in SExtractor. Since the GRAPES spectra were extracted in a trace of fixed width (Pirzkal et al. 2004), they must be scaled to reproduce the fluxes measured by SExtractor in the HUDF. Therefore, we define a multiplicative aperture correction as $\beta = 10^{-0.4(i'_{\rm HUDF} - i'_{\rm GRAPES})}$, where $i'_{\rm HUDF}$ and $i'_{\rm GRAPES}$ are the i'-band magnitudes measured from the ACS imaging and the GRAPES spectra, respectively. Since the i'-band image was used to define the apertures used in the other images, there is no need for additional corrections between the broadband images.

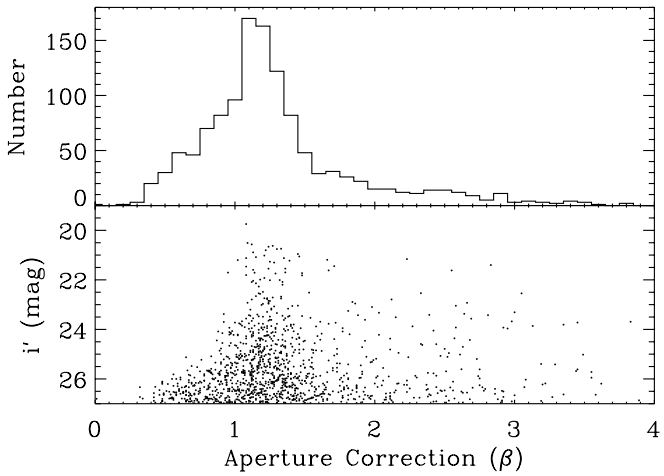

FIG. 1.—Aperture corrections for the 1308 GRAPES galaxies. The aperture correction is defined such that the GRAPES spectra reproduce the i'-band fluxes measured from the HUDF. Since the NUV and NIR fluxes are measured with apertures defined by the i'-band data, there are no additional corrections between the broadband data. *Top*: Distribution of aperture corrections. The GRAPES spectra are only scaled to reproduce the i'-band fluxes, since their usable portion does not completely cover the neighboring bandpasses (V and z'). *Bottom*: Dependence of the i'-band magnitude on the aperture correction. The majority of the objects with $\beta \leq 1$ are near the detection limit of $i' \simeq 27$ mag. This suggests that uncertainties in the background subtraction may be the cause of these aperture corrections (Pirzkal et al. 2004).

The distribution of these aperture corrections is shown in Figure 1. The width of this distribution is related to the properties of the spectral extraction, contamination of nearby objects, and the broadband apertures. Since the GRAPES spectra are most reliable from ~6000 to 9500 Å, they do not fully cover the V or z' bands; therefore, scaling to multiple bands or using a wavelength-dependent aperture correction is not possible with these data. Lastly, the scaled GRAPES spectra are rebinned onto a common wavelength grid and are assigned a 100 Å wide top-hat filter transmission curve. This procedure typically decreases the number of GRAPES spectral points by a factor of ~2 and boosts their signal-to-noise ratio, which markedly helps for the faintest sources ($i' \simeq 27$ mag).

3. SPECTROPHOTOMETRIC REDSHIFTS

Measuring redshifts from a calibrated spectrum requires readily identifiable absorption or emission lines or characteristic breaks. Since the GRAPES data have a resolution of $R \simeq 100$, the narrow spectral features are typically not detectable. Xu et al. (2007) measured emission-line redshifts from ~100 GRAPES galaxies; therefore, we complement that study by estimating spectrophotometric redshifts for the remaining data set from the low-resolution GRAPES spectra.

From the scaled spectra and broadband fluxes, we compute spectrophotometric redshifts with the code HyperZ (Bolzonella et al. 2000). The alternative code, BPZ (Benítez 2000), was not used for three reasons: it currently does not constrain the galaxy ages to be less than the age of the universe, it does not compute many useful secondary quantities, and, with our spectral constraints and coverage, BPZ is not expected to substantially outperform HyperZ. Mobasher et al. (2004) compares the quality of redshifts from HyperZ and BPZ for a sample of $\simeq$400 galaxies in the Chandra Deep Field–South using broadband fluxes. They show that the

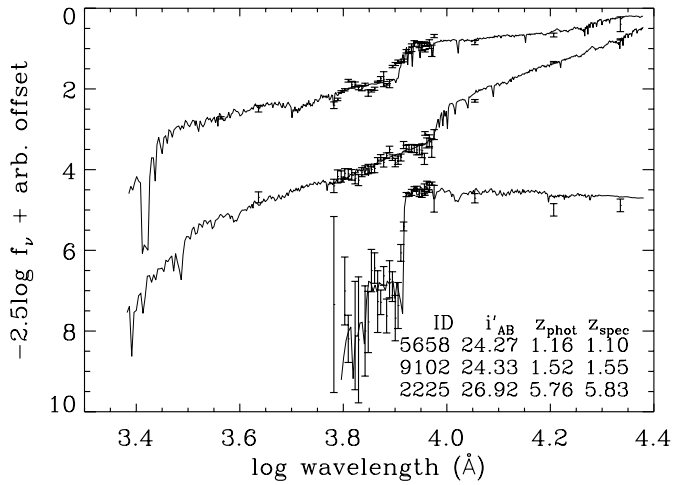

FIG. 2.—Representative SEDs. These examples highlight two advantages of the GRAPES data: high signal-to-noise ratio at faint flux levels ($i' \sim 25$ mag) and excellence in determining spectral breaks. In the lower right corner, we tabulate the HUDF ID, the i'-band magnitude, the spectrophotometric redshift derived in this work, and the published spectroscopic redshift. The spectra are arranged in descending redshift, so from top to bottom the IDs are 5658, 9102, and 2225. With the addition of the Wide Field Camera 3 (WFC3) on the *HST*, we can expect UV prism and IR grism data at 1900–4500 Å and 1.1–1.7 μm, respectively. The combination of ACS and WFC3 spectra will provide an extremely broad spectral coverage at low–medium resolution.

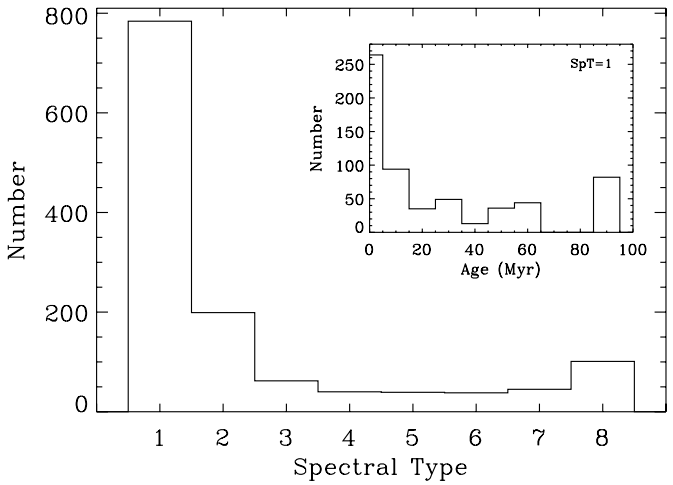

FIG. 3.—Distribution of BC03 spectral types. Clearly the burst template is the dominant SED, and from the inset, we see that these galaxies are typically very young. This is somewhat expected, since the majority of galaxies at $z \sim 1$ are young and actively forming stars. Since the BC03 templates are tabulated as a function of stellar population age, we require that this age be less than the age of the universe at the given redshift.

rms scatter in the photometric redshifts is 0.140 and 0.072 for χ^2 and Bayesian techniques, respectively. In Figure 2, we show three observed SEDs with best-fit templates where there is reasonable agreement between our redshift and the published value. These examples illustrate the power of the GRAPES spectra to locate the 4000 Å break (*upper and middle SEDs*) and the Lyα break (*lower SED*).

Using the set of SED templates summarized in Table 1, HyperZ minimizes the reduced χ^2 between the observed and modeled fluxes as a function of redshift, age, and extinction. By neglecting the $Vi'z'$ bands in the spectrophotometric redshift calculation, the combination of scaled GRAPES spectra and remaining broadband fluxes typically yields $\simeq$40 fully independent spectral bins per galaxy. In Figure 3 we show the distribution of best-fit spectral types for the 1308 galaxies. Since the Bruzual & Charlot (2003, hereafter BC03) templates are generated at a series of finite time steps of $\Delta \log (t/1\ \mathrm{Gyr}) \lesssim 0.05$, we require the galaxy to be less than the age of the universe at a given redshift. Template 1 (the "burst" template) describes a single instantaneous burst followed by passive stellar evolution. Since this template is the most common, we show the distribution of stellar ages in the inset. We see that the majority of the burst models are very young, which is not surprising, since galaxies are expected to be blue and actively forming stars at $z \sim 1$ (e.g., Xu et al. 2007).

TABLE 1
HyperZ TEMPLATES

Spectral Type[a]	τ[b] (Gyr)
1	0
2	1
3	2
4	3
5	5
6	15
7	30
8	∞

[a] All of the templates came from the BC03 stellar population synthesis models assuming an exponential star formation history.
[b] The quantity τ is the *e*-folding time in the exponential function.

4. RESULTS

4.1. *Redshift Quality*

We compare our spectrophotometric redshifts to the published spectroscopic measurements (Grazian et al. 2006; Ravikumar et al. 2007; Vanzella et al. 2006). Of the 1308 GRAPES galaxies, only 114 have measured spectroscopic redshifts. For these galaxies, we show the fractional error in $1 + z$ as a function of the spectroscopic redshift in Figure 4. The top and bottom left panels show the error for different sets of fluxes used in the redshift computation, as indicated in the upper right corners of the left panels. Photometric redshifts are the most reliable when a readily identifiable spectral break occurs between two adjacent bandpasses. The 4000 Å and Lyα breaks will occur in the GRAPES spectra for $0.5 \leq z \leq 1.5$ and $4 \leq z \leq 8$, respectively. Therefore, when either of these breaks occur in the GRAPES spectra, we expect accurate redshifts. The standard deviation of the fractional error is 0.051 for redshifts computed using only the broadband observations. However, when we use the low-resolution grism in place of the $Vi'z'$ bandpasses, the overall redshift uncertainty is reduced to 0.037 for the 75 galaxies with $0.5 \leq z \leq 1.5$. Since these low-resolution spectra eliminate the need for deep V and z' imaging, this approach requires $\sim$10% of the observing time while producing more accurate redshifts and providing more spectral information. In Table 2, we show a representative portion of the final catalog. The entire machine-readable version is available online.

4.2. *Luminosity Functions*

We calculate the LF using the $V_{\max}$ method (Schmidt 1968; Willmer 1997) in 1.0 mag wide bins from absolute magnitudes measured from HyperZ by convolving the best-fit spectrum with the rest-frame *B* bandpass. We construct three redshift intervals:

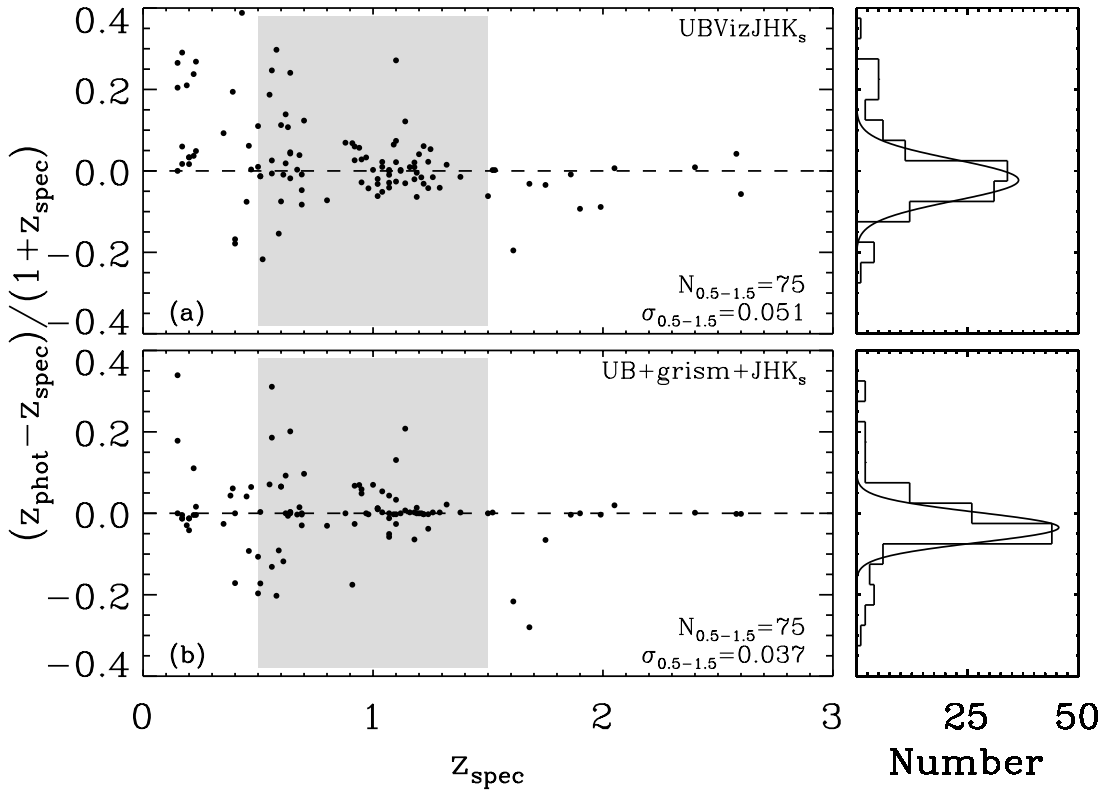

FIG. 4.—Comparison between GRAPES spectrophotometric and spectroscopic redshifts from the VLT (Grazian et al. 2006; Ravikumar et al. 2007; Vanzella et al. 2006). The schemes for computing the redshifts are indicated in the upper right corners of the left panels. We tabulate the standard deviation of the fractional error in $1+z$ for the shaded redshift range $0.5 \leq z \leq 1.5$, which is when the 4000 Å break occurs in the grism spectra, and the number of galaxies in the lower right corners of the left panels. The distribution of the residuals is shown in the right panels. Seven catastrophic outliers have been eliminated, since they contained strong emission lines (Xu et al. 2007), which are not accounted for in the stellar population synthesis models. While the broadband data alone can yield good redshift estimates, with the low-resolution grism spectra we further refine the redshifts to $\sigma_{0.5-1.5} = 0.037$. Since these data constitute the extreme case of the best possible data (ultradeep ACS and NICMOS imaging), the redshift refinement is only marginal. However, we expect a much more substantial improvement in the more general case of shallower imaging without broad spectral coverage.

$z = 1.0 \pm 0.2$, which has the best statistics, $z = 0.9 \pm 0.1$, and $z = 1.1 \pm 0.1$ for direct comparison to previous studies. The differential LF is then computed by $\Phi(M)\,dM = N(M)\,dM/\Delta V(z_{\max})$, where $N(M)\,dM$ is the number of galaxies with absolute magnitudes between M and $M + dM$ and

$$\Delta V(z_{\max}) = \frac{\Omega}{4\pi} \int_{z_{\min}}^{z_{\max}} C(z, M)\, \frac{dV}{dz}\, dz, \qquad (1)$$

where Ω is the solid angle of the GRAPES survey, $z_{\max}$ is the maximum redshift at which a galaxy with an absolute magnitude of M_B would have been detected in the survey, and $C(z, M_B)$ is the completeness function. The uncertainties on $\Phi(M)\,dM$ are computed with the assumption of Poisson noise from the galaxy counts (e.g., Wolf et al. 2003).

To estimate the completeness in each absolute magnitude bin, we use a Monte Carlo simulation (Wolf et al. 2003; Budavári et al. 2005). First, we generate random redshifts from a Gaussian distribution of width 0.037, as expected from Figure 4. Next, we count the number of deviates with apparent magnitudes brighter than the survey limit and take the ratio of the number recovered to the number simulated as the completeness. This correction is typically less than a factor of 10 for the absolute magnitudes presented.

In Figure 5, we show the LFs for $z = 0.90 \pm 0.10$ (*left*) and $z = 1.10 \pm 0.10$ (*right*). We model these LFs with a standard Schechter function (Schechter 1976), which is parameterized by the normalization (Φ^*), the characteristic absolute magnitude (M^*), and the faint-end slope (α). Also in Figure 5, we show the contours for $\Delta\chi^2_\nu = 1, 4$, and 9 in the α-M^* plane as insets. While

TABLE 2
SPECTROPHOTOMETRIC REDSHIFT CATALOG

HUDF ID[a]	x (pixels)	y (pixels)	R.A. (J2000)	Decl. (J2000)	i' (mag)	β	$z_{\rm phot}$	SpT	Age (Gyr)	M_B (mag)
1.....	4932.88	802.89	3 32 39.7	−27 49 42.5	22.931 ± 0.012	1.14	0.38	5	7.500	−17.75
5.....	5089.39	753.56	3 32 39.4	−27 49 44.0	26.983 ± 0.110	0.60	0.69	1	0.090	−14.36
7.....	5052.73	788.94	3 32 39.5	−27 49 42.9	25.367 ± 0.030	1.21	0.61	1	0.004	−16.96
8.....	5013.85	1274.58	3 32 39.5	−27 49 28.4	21.464 ± 0.003	1.14	0.64	1	1.434	−20.18
13.....	5108.60	918.70	3 32 39.3	−27 49 39.1	24.985 ± 0.042	1.76	0.52	1	0.360	−16.62

NOTES.—Units of right ascension are hours, minutes, and seconds, and units of declination are degrees, arcminutes, and arcseconds. Table 2 is presented in its entirety in the electronic edition of the *Astrophysical Journal*. A portion is shown here for guidance regarding its form and content.

[a] Identification from Beckwith et al. (2006).

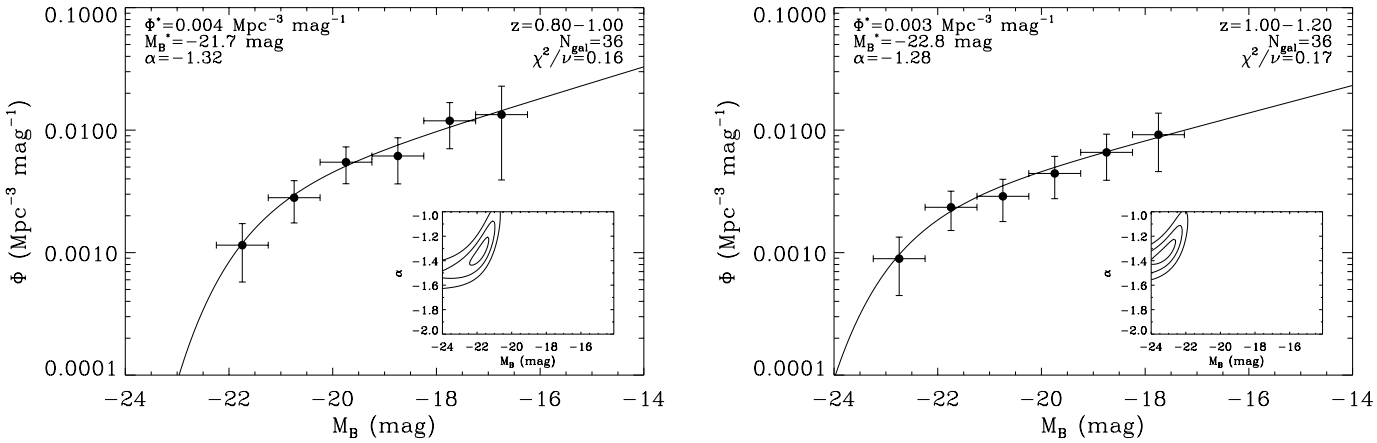

FIG. 5.—Two *B*-band luminosity functions for $z = 0.8$–1.0 (*left*) and $z = 1.0$–1.2 (*right*), with corresponding $\Delta\chi^2_\nu$ contours in the α-M^* plane. The offset and scatter in Fig. 4 will only alter the absolute magnitudes by $\Delta M \simeq 0.1$ mag at these redshifts. Due to the faint flux limit of the GRAPES survey ($i' = 27.2$ mag), we are able to directly determine the Schechter parameters in this critical redshift interval for galaxy evolution. While these data can accurately determine $M^* = -22.4 \pm 0.3$ and $\alpha = -1.32 \pm 0.07$ (for $z = 1.0 \pm 0.2$), the normalization (Φ^*) is less certain, since the object selection and contamination in grism spectroscopy poses significant challenges. Therefore, the union of complete ground-based surveys with these deep grism observations provides the most thorough results.

the total number of galaxies in these redshift bands may be low ($\sim$10 galaxies per absolute magnitude bin), the GRAPES data set provides excellent constraints of the Schechter parameters (see Table 3). Previous studies at these redshifts often used ground-based spectroscopic surveys, which are inherently limited to $M_B \sim -19$ mag (such as Chen et al. 2003; Abraham et al. 2004; Cross et al. 2004; Zucca et al. 2006). Consequently, it has been customary to *assume* a faint-end slope of $\alpha \simeq -1.3$ (e.g., Willmer et al. 2006). However, the GRAPES observations provide a means to *measure* the faint-end slope of $\alpha = -1.32 \pm 0.07$ at $z = 1.0 \pm 0.2$. It is reassuring that the assumption of $\alpha \simeq -1.3$ at these redshifts is not wholly incorrect.

4.3. *Redshift Evolution of the Faint-End Slope*

The hierarchical formation scenario states that many dwarf galaxies at high redshift will merge over cosmic time, which results in a increased number of dwarf galaxies at high redshift. This effect could be observed as a steepening of the faint-end slope with redshift. In Figure 6 we show the redshift dependence of the faint-end slope compiled from numerous studies. These studies include, but are not limited to, the largest ground-based redshift surveys (e.g., Norberg et al. 2002; Blanton et al. 2003), the deepest *HST* surveys (e.g., Beckwith et al. 2006), and nearby *GALEX* surveys (e.g., Budavári et al. 2005; Wyder et al. 2005). While each survey has unique selection effects and observational biases, many problems can be mitigated by requiring two criteria of the data set: a sufficient amount of data *fainter* than M^* and a minimal reliance on *k*-corrections. Ilbert et al. (2004) emphasize that only surveys for which $1 + z_{\rm obs} \sim \lambda^S/\lambda^{\rm ref}$ (where $z_{\rm obs}$ is the redshift of the LF and λ^S and $\lambda^{\rm ref}$ are the wavelengths at which the galaxies are selected and the LF is computed, respectively) can reliably infer the faint-end slope. When the Ilbert et al. (2004) condition is met, the *k*-correction is minimized. For uniformity, we only show values of α that meet these requirements. In Figure 6, the red and blue circles indicate the faint-end slopes measured in the rest-frame *B* band and far-UV (FUV $\simeq$ 1700 Å), respectively. Our GRAPES observation is indicated as a filled red circle at $z = 1.0 \pm 0.2$.

From Figure 6, the faint-end slope clearly depends on redshift in the manner suggested in the hierarchical scenario: many low-mass galaxies at high redshift, which, throughout cosmic time, merge into the massive galaxies of today. We parameterize the redshift dependence of the faint-end slope as $\alpha(z) = a + bz$ and give the best-fit models for the entire data set and for the FUV as

TABLE 3
BEST-FIT SCHECHTER PARAMETERS

z	$N_{\rm gal}$	Φ^* (10^{-4} Mpc^{-3} mag^{-1})	M_B^* (mag)	α
0.90 ± 0.10.....	36	35.9 ± 0.2	-21.7 ± 0.9	-1.32 ± 0.19
1.10 ± 0.10.....	36	25.8 ± 0.1	-22.8 ± 0.5	-1.28 ± 0.10
1.00 ± 0.20.....	72	26.1 ± 0.1	-22.4 ± 0.3	-1.32 ± 0.07

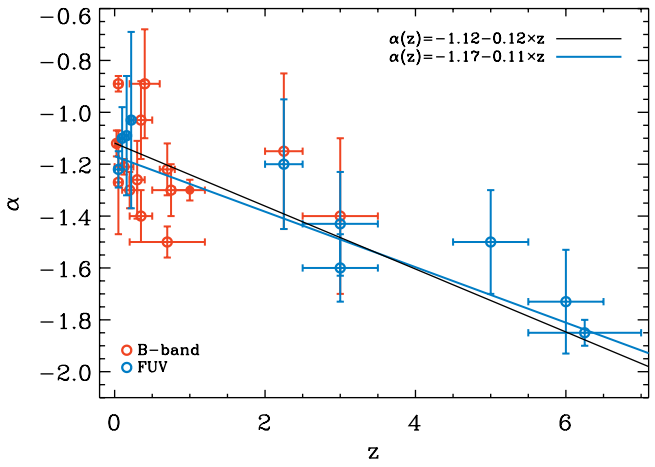

FIG. 6.—Compendium of the faint-end slope values for the galaxy luminosity function. We show 23 published slopes from 18 sources, including this work. While there are many more values, we require each survey to have measured the LF to $\sim$2 mag fainter than M^* and, optimally, to have selected their galaxies to minimize the *k*-correction (Ilbert et al. 2004) to ensure uniform and reliable estimates of the faint-end slope. The red circles indicate the measurements made in the rest-frame *B* band (Lilly et al. 1995; Lin et al. 1997; Sawicki et al. 1997; Marzke et al. 1998; Fried et al. 2001; Norberg et al. 2002; Blanton et al. 2003; Driver & de Propris 2003; Wolf et al. 2003; Marchesini et al. 2007; Scarlata et al. 2007), the blue circles represent the rest-frame FUV (Steidel et al. 1999; Iwata et al. 2003; Yan & Windhorst 2004; Budavári et al. 2005; Wyder et al. 2005; Bouwens et al. 2006; Sawicki & Thompson 2006), and the filled red circle at $z = 1.0 \pm 0.2$ is the result from this work. This suggests that dwarf galaxies were more numerous at high redshift, as predicted in the hierarchical formation paradigm.

black and blue lines, respectively, in Figure 6. While the two fits are consistent with each other and the observations, the significant scatter warrants further study. There are many effects that could contribute to this scatter: differences in the rest-frame bandpass, type-dependent evolution, galaxy clustering and large-scale structure, and nonuniform sample selections.

5. DISCUSSION

We present a catalog of 1308 spectrophotometric redshifts for the objects observed in the GRAPES project. When the GRAPES spectra are supplemented with $UJHK_s$ fluxes from other facilities, the standard deviation of the fractional error in $1 + z$ for the 75 GRAPES galaxies in the redshift range $0.5 \leq z \leq 1.5$ is 0.037. While this is only a marginal improvement over traditional photometric redshifts, it requires $\sim$10% of the exposure time. Since the photometric redshift technique is essentially a "break-finding" algorithm, the redshift accuracy of the GRAPES observations is limited by the spectral resolution of the grism. Therefore, we can estimate spectrophotometric redshifts at a comparable depth and accuracy with only $\simeq$50 orbits with *HST* (40 orbits for the grism observations and 10 orbits for an i'-band exposure for object selection). This is a critical improvement for wide-angle surveys, which may be completely reliant on traditional photometric redshifts. Moreover, the grism observations provide a necessary complement to the deep, ground-based spectroscopic surveys. Due to the line-spread function and resolution of the grism spectra, determining redshifts from emission lines in a fashion similar to ground-based observations is typically not possible. However, from the high signal-to-noise ratio continua, the spectral breaks found at flux levels not achievable from the ground can provide excellent redshift measurements.

Since the *HST* ACS grism observations allow for significantly deeper spectral observations, we are able to measure the faint end of the *B*-band luminosity function at redshifts not currently possible from the ground. In the hierarchical formation scenario, galaxies are expected to evolve by successive merging over cosmic time. Therefore, we expect to find fewer dwarf galaxies at lower redshifts, which can be measured in terms of the evolution of the Schechter parameters. These data are able to measure the faint-end slope in the critical redshift range of $z = 0.5$–1.5, where the cosmic star formation rate is substantially changing. When our faint-end slope is compared to numerous studies, we find strong evidence for a redshift-dependent value of α. While previous authors have suggested a similar trend (e.g., Arnouts et al. 2005; Zucca et al. 2006), the compilation of published results provides an increase in both statistics and redshift range.

The redshift dependence of the other two Schechter parameters has been discussed by other authors. Lin et al. (1999) study the redshift evolution of the *B*-band galaxy LF and in particular propose the parameterizations of $M^*(z) = M^*(0) - Qz$ and $\rho(z) = \rho(0)10^{0.4Pz}$, where $\rho = \int \Phi(M)\, dM$. If α is constant with redshift, then ρ and Φ^* are essentially equivalent. The parameters P and Q provide a simple way of quantifying galaxy evolution and can be determined as a function of galaxy type. For $q_0 = 0.1$, Lin et al. (1999) find $(P, Q) = (-1.00 \pm 0.40, 1.72 \pm 0.41)$ for the combination of early- and intermediate-type galaxies. Fried et al. (2001) parameterize Φ^* linearly on redshift: $\Phi^*(z) = a + b(1 + z)$, where there is only a minimal dependence of galaxy type on the coefficients a and b. From the observed redshift evolution of the Schechter parameters, an obvious trend is emerging: the galaxy LF is shallower and has a brighter characteristic absolute magnitude at low redshifts.

The improvement with the grism spectroscopy over traditional photometric redshifts on a per observation basis bears strongly on future NASA missions, such as the Wide Field Camera 3 upgrade for the *Hubble Space Telescope* and the planned *James Webb Space Telescope*.

We thank the anonymous referee for the many suggestions that improved the paper. We acknowledge the support from the Arizona State University NASA Space Grant (to R. E. R.). This work was supported by grants GO 9793 and GO 10530 from the Space Telescope Science Institute, which is operated by AURA under NASA contract NAS 5-26555. The work of L. A. M. and J. D. R. was carried out at the Jet Propulsion Laboratory, California Institute of Technology, under a contract with NASA.

REFERENCES

Abraham, R. G., et al. 2004, AJ, 127, 2455
Arnouts, S., et al. 2005, ApJ, 619, L43
Beckwith, S. V. W., et al. 2006, AJ, 132, 1729
Benítez, N. 2000, ApJ, 536, 571
Bertin, E., & Arnouts, S. 1996, A&AS, 117, 393
Blanton, M. R., et al. 2003, ApJ, 592, 819
Bolzonella, M., Miralles, J.-M., & Pelló, R. 2000, A&A, 363, 476
Bouwens, R. J., Illingworth, G. D., Blakeslee, J. P., & Franx, M. 2006, ApJ, 653, 53
Bruzual, G., & Charlot, S. 2003, MNRAS, 344, 1000 (BC03)
Budavári, T., et al. 2005, ApJ, 619, L31
Caputi, K. I., Dunlop, J. S., McLure, R. J., & Roche, N. D. 2004, MNRAS, 353, 30
Chen, H.-W., et al. 2003, ApJ, 586, 745
Coe, D., Benítez, N., Sánchez, S., Jee, M., Bouwens, R., & Ford, H. 2006, AJ, 132, 926
Cross, N. J. G., et al. 2004, AJ, 128, 1990
Driver, S., & de Propris, R. 2003, Ap&SS, 285, 175
Ferguson, H. C. 1999, in ASP Conf. Ser. 191, Photometric Redshifts and the Detection of High Redshift Galaxies, ed. R. Weymann et al. (San Francisco: ASP), 51
Fernández-Soto, A., Lanzetta, K. M., & Yahil, A. 1999, ApJ, 513, 34
Fried, J. W., et al. 2001, A&A, 367, 788
Grazian, A., et al. 2006, A&A, 449, 951
Ilbert, O., et al. 2004, MNRAS, 351, 541
Iwata, I., Ohta, K., Tamura, N., Ando, M., Wada, S., Watanabe, C., Akiyama, M., & Aoki, K. 2003, PASJ, 55, 415
Lanzetta, K. M., Yahil, A., & Fernández-Soto, A. 1996, Nature, 381, 759
Lilly, S. J., Tresse, L., Hammer, F., Crampton, D., & Le Fèvre, O. 1995, ApJ, 455, 108
Lin, H., Yee, H. K. C., Carlberg, R. G., & Ellingson, E. 1997, ApJ, 475, 494
Lin, H., Yee, H. K. C., Carlberg, R. G., Morris, S. L., Sawicki, M., Patton, D. R., Wirth, G., & Shepherd, C. W. 1999, ApJ, 518, 533
Marchesini, D., et al. 2007, ApJ, 656, 42
Marzke, R. O., da Costa, L. N., Pellegrini, P. S., Willmer, C. N. A., & Geller, M. J. 1998, ApJ, 503, 617
Mobasher, B., et al. 2004, ApJ, 600, L167
———. 2007, ApJS, 172, 117
Norberg, P., et al. 2002, MNRAS, 336, 907
Oke, J. B., & Gunn, J. E. 1983, ApJ, 266, 713
Pirzkal, N., et al. 2004, ApJS, 154, 501
Ravikumar, C. D., et al. 2007, A&A, 465, 1099
Riess, A. G., et al. 2004, ApJ, 600, L163
Sawicki, M., & Thompson, D. 2006, ApJ, 642, 653
Sawicki, M. J., Lin, H., & Yee, H. K. C. 1997, AJ, 113, 1
Scarlata, C., et al. 2007, ApJS, 172, 406
Schechter, P. 1976, ApJ, 203, 297
Schmidt, M. 1968, ApJ, 151, 393
Spergel, D. N., et al. 2007, ApJS, 170, 377
Stanway, E. R., Bunker, A., & McMahon, R. G. 2003, Ap&SS, 284, 381
Steidel, C. C., Adelberger, K. L., Giavalisco, M., Dickinson, M., & Pettini, M. 1999, ApJ, 519, 1
Thompson, R. I., et al. 2005, AJ, 130, 1
Vanzella, E., et al. 2006, A&A, 454, 423

Williams, R. E., et al. 1996, AJ, 112, 1335
Willmer, C. N. A. 1997, AJ, 114, 898
Willmer, C. N. A., et al. 2006, ApJ, 647, 853
Wolf, C., Meisenheimer, K., Rix, H.-W., Borch, A., Dye, S., & Kleinheinrich, M. 2003, A&A, 401, 73
Wyder, T. K., et al. 2005, ApJ, 619, L15
Xu, C., et al. 2007, AJ, 134, 169
Yan, H., & Windhorst, R. A. 2004, ApJ, 612, L93
Zucca, E., et al. 2006, A&A, 455, 879